

Chu-Limit-Guided Decomposition-Based Multiobjective Large-Scale Optimization for Generative Broadband Electrically Small Antenna Design

Yu Kuang, *Graduate Student Member, IEEE*, Qingsha S. Cheng, *Senior Member, IEEE* and Zhi Ning Chen, *Fellow, IEEE*

Abstract—In traditional electrically small antennas (ESAs) design frameworks, overcoming the bandwidth limit derived from the Chu limit is considered unachievable. This paper proposes a three-dimensional (3-D) ESA configuration with high degrees of freedom (DoF), which is employed to significantly expand the design space for beyond-limit solutions. A revised multiobjective evolutionary algorithm based on decomposition (MOEA/D) is presented, which is guided by a Pareto front derived from the bandwidth limit to achieve rapid convergence. Prior knowledge, including structural priors, fabrication constraints, and physical interpretations of design parameters and objectives, is incorporated to efficiently generate effective solutions. The proposed method generates nine solutions, all of which exceed the bandwidth limits. A “radial-beamlet” antenna, fabricated using metal 3-D printing, achieves impedance bandwidth of 50.3% (2.05–3.43 GHz) and realized gain of 1.72–3.86 dBi. The bandwidth-efficiency product of the fabricated solution is 0.402, compared to the performance limit of 0.389. This approach pushes the boundaries of electrically small antennas and provides a new pathway for the advanced design of similar structures.

Index Terms—Electrically small antenna, Metal 3D printing, Chu limit, Multi-objective, Optimization.

I. INTRODUCTION

Broadband omnidirectional electrically small antennas (ESAs) are essential in practical wireless devices such as portable terminals, IoT nodes, wearable sensors, and compact communication modules. The Wheeler and Chu limits [1],[2] define a fundamental constraint on the performance of ESAs, quantifying the trade-off between electrical size and the quality

Manuscript received xx xx, 2025. This work was supported in part by the National Natural Science Foundation of China under Grant 62071211, in part by the Shenzhen Science and Technology Program under Grant JCYJ20240813095713018, and in part by the Advanced Research and Technology Innovation Centre (ARTIC), National University of Singapore, under Grant AFP-RP1. (*Corresponding author: Qingsha S. Cheng*.)

Yu Kuang is with the Department of Electrical and Electronic Engineering, Southern University of Science and Technology, Shenzhen 518055, China, and also with the Department of Electrical and Computer Engineering, National University of Singapore, Singapore 117583 (e-mail: kuangyu@u.nus.edu).

Qingsha S. Cheng is with the Department of Electrical and Electronic Engineering, Southern University of Science and Technology, Shenzhen 518055, China (e-mail: chengqs@sustech.edu.cn).

Zhi Ning Chen is with the Department of Electrical and Computer Engineering, National University of Singapore, Singapore 117583 (e-mail: eleczn@nus.edu.sg).

(Q) factor, which is practically related to the product of fractional bandwidth and radiation efficiency [3]. The size of the antenna is defined by the product, ka , where k is the wavenumber at the center frequency and a is the radius of the minimum sphere enclosing the antenna. The theoretical limit has been explored from various perspectives, including circuit quantities[1]-[5], field quantities[6],[7], and source current analyses[8]-[10], focusing on the fundamental principles rather than specific antenna implementations.

To make these theoretical limits relevant to practical antenna design, validation in practical implementations is essential. Studies have shown that spherical helix structures can nearly achieve the optimal current distributions for spherical shells [11]-[13]. Similarly, several TM dipole antennas have been shown to closely approach the performance limits for planar and cylindrical geometries [8],[14],[15]. Although achieving the Chu bound remains challenging, numerous approaches have been proposed to tackle this issue [16]-[19]. A comprehensive survey [20] on small antenna designs highlights the substantial gap between existing designs and the performance limit.

Artificial intelligence (AI) and optimization techniques have played a critical role in advancing the design of increasingly complex antennas to meet stringent specifications. Heuristic optimization methods, such as genetic algorithms (GA) [21] and particle swarm algorithms (PSO) [22], are exploited to explore unintuitive three-dimensional (3-D) antenna configurations. However, their limited degree-of-design freedom (DoF) makes it challenging to approach the performance limit. In contrast, numerical current-based design approaches offer improved proximity to theoretical limits for ESAs [23]-[27], thanks to their ability to converge under extremely high DoF, enabling optimal current distributions on predefined surfaces.

Building on this idea, generative design, which involves creating high DoF antenna configuration, has emerged as a powerful approach to exploring unconventional and high-performance designs. For example, increasing the DoF in unit cell design has led to phase breakthroughs in metasurfaces, thereby enhancing the metalens performance [28]-[30]. Likewise, expanding the DoF in 3D ESA configurations offers the potential to reach the performance limit by enhancing the design flexibility. However, this also significantly increases the

complexity of the optimization problem, introducing challenges associated with large-scale design spaces and computational efficiency.

The design space increases exponentially with the number of design parameters, a phenomenon known as “curse of dimensionality” in numerical optimization [31]. Meanwhile, the inherently conflicting objectives in antenna design, including bandwidth, efficiency, and size, define it as a high-dimensional multiobjective optimization problem (MOP). The multiobjective evolutionary algorithm based on decomposition (MOEA/D) [32] is a mainstream method in solving MOPs. In antenna applications, most MOEA/D-based studies focus on tailoring reproduction operators and update strategies to improve performance in specific scenarios [33]-[35] and aiming to balance convergence speed and solution diversity [36],[37]. However, few existing approaches are tailored to high-dimensional antenna optimization problems and lack convergence guidance based on physical insights.

The Wheeler and Chu limits represent the Pareto front of the MOP that seeks to simultaneously maximize the fractional bandwidth and minimize electrical size. This study incorporates such prior knowledge, together with other empirical experience, into the MOEA/D framework to enhance convergence efficiency in large-scale optimization problems.

This paper proposes a Chu limit-guided decomposition-based multiobjective large-scale optimization technique for generative design of broadband ESAs. A high DoF 3-D ESA configuration is proposed. The Pareto front derived from the performance limit, together with other physical knowledge, are employed to guide problem decomposition, initialization, and reproduction, enabling more efficient convergence in the high-dimensional design space. The proposed ESA configuration is further optimized under prior knowledge constraints to validate the effectiveness of the algorithm. Nine solutions exceeding performance limit are obtained in the population of the 20th generation. One of the solutions is simplified, fabricated using the 3-D printing, and experimentally measured.

The main contributions of this paper are as follows:

- 1) A novel problem decomposition strategy in MOEA/D that leverages the true Pareto front derived from theoretical limits and engineering constraints, enabling direct convergence guided by prior knowledge.
- 2) Integration of additional prior knowledge into initialization and reproduction processes to efficiently generate effective and feasible solutions, further enhancing convergence in large-scale optimization of a 3-D ESA with high degrees of freedom.
- 3) A systematic generative-design framework is proposed that consistently generates beyond-limit solutions on a unified ESA configuration, with experimental validation through an equivalent fabricated prototype. This confirms that approaching the performance limit is a repeatable and systematically achievable engineering capability.

II. GENERATIVE ANTENNA DESIGN CONCEPT, HIGH DOF CONFIGURATION AND MOP FORMULATION

This section presents the concept of generative antenna

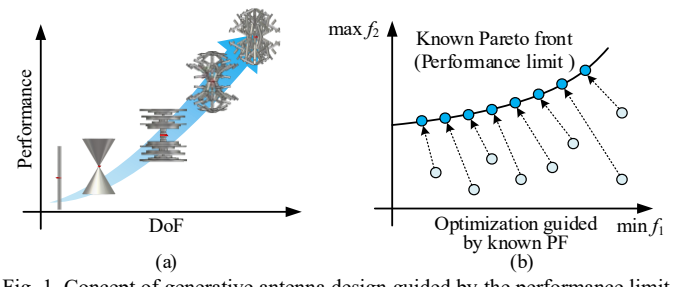


Fig. 1. Concept of generative antenna design guided by the performance limit. (a) Increasing antenna DoF to improve performance. (b) Performance limit transformed into a known PF guiding multiobjective optimization.

design (GAD). Guided by this concept, the 3-D ESA configuration with high-DoF is developed and a large-scale multiobjective optimization problem is formulated.

A. Concept: Generative Antenna Design using Optimization

Generative antenna design (GAD) aims to explore novel high-DoF antenna structures through optimization, approaching performance limits guided by prior knowledge. The GAD concept, as shown in Fig. 1, includes two key features: (1) significantly increasing the DoF in antenna configuration to expand the design space, and (2) integrating prior knowledge to guide optimization towards performance limit.

The objective of increasing DoF in antenna design is to significantly expand the design space, enabling the generation of new designs with excellent performance. The DoF typically includes geometry parameters, configurations, and structures. As shown in Fig. 1(a), representative antenna structures with increasing DoF demonstrate a clear progression in performance. The increase of DoF provides greater design diversity and design flexibility but also introduces challenges for optimization due to the vast design space.

Incorporating prior knowledge (PK) in algorithms is to achieve efficient convergence to multiple feasible designs. Prior knowledge generally includes engineering constraints, fundamental electromagnetic theory, and empirical experience. As shown in Fig. 1(b), the performance limit derived from the Chu limit is transformed into the known Pareto front. This PF is embedded into the optimization process to guide problem decomposition and solution assignment, thereby improving convergence toward high-performance designs.

B. 3-D ESA Configuration with High DoF

To effectively increase the DoF of the ESA, the proposed configuration consists of multiple metal rods arranged at fixed positions around a center-fed dipole. The existence and orientation of each rod are optimized to create a complex parasitic loading configuration. The modeling description is shown in Fig. 2. 27 customized positions are determined uniformly distributed within one-eighth spherical regions, as shown in Fig. 2(a). The radius of the enclosing spherical regions is a . The radius r , length l , and rotation angles (ϕ and θ) in azimuth and elevation planes of each metal rod define its posture, as shown in Fig. 2(b). A D_4 symmetry around the z -axis and a horizontal mirror symmetry across the xoy plane are applied as symmetric constraints. These constraints enforce the lowest-order TM_{10} spherical-mode behavior and effectively

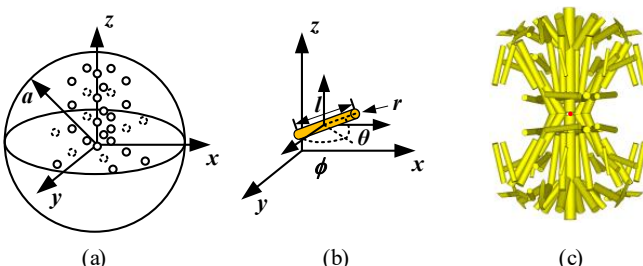


Fig. 2. Geometry modelling of the antenna. (a) Customized rod positions within one of the eight spherical regions. (b) Configuration of a rod around driven dipole. (c) The proposed 3-D ESA configuration in simulation.

reduce the design DoF. One possible generated structure is illustrated in Fig. 2(c). This configuration is fed through a 50Ω discrete port (red dot) positioned at the center between the arms of the driven dipole in the simulation. Compared to low-DoF geometry-based models and high-DoF voxel-based models, it provides an intermediate level of DoF that is sufficient to generate complex parasitic structures without being too challenging for algorithms.

C. Problem Formulation

Following the concept of GAD, approaching the performance limit of the ESA based on the proposed 3-D configuration can be formulated as a multiobjective optimization problem. The two conflict objectives are electrical size ka and fractional bandwidth BW . The optimization problem to be solved can be described as follows:

$$\begin{aligned} \min \mathbf{F}(\mathbf{x}) = & (f_1(\mathbf{x}^b, \mathbf{x}^c), -f_2(\mathbf{x}^b, \mathbf{x}^c)) \\ \text{w.r.t. } & \mathbf{x}^b \in R^m, \mathbf{x}^c \in R^n \\ \text{s.t. } & x_i^b \in \{0,1\}, x_j^c \in [L_j^c, U_j^c] \end{aligned} \quad (1)$$

where \mathbf{F} is a vector of two objective functions. \mathbf{x}^b is a vector of binary variables indicating whether a metal rod is present at each specific position, with '1' representing the presence of a rod and '0' representing its absence. m is the dimension of binary variables. \mathbf{x}^c is a vector of continuous variables, representing the posture of metal rods, including length, radius, and rotate angles. n is the dimension of continuous variables, corresponding to the number of metal rods present, as indicated by the number of "1" in \mathbf{x}^b . f_1 and f_2 denote the objective functions for center frequency and fractional bandwidth, respectively. \mathbf{L}^c and \mathbf{U}^c define the lower and upper bounds of \mathbf{x}^c .

The formulated problem features: (1) *Large scale*: 135 design parameters in total; (2) *Mixed-variable structure*: the design parameters typically include binary and continuous types. (3) *Variable-length design space*: the dimension of the continuous parameters varies from 4 to 108, defined by the binary parameters. (4) *Expensive optimization*: each EM full-wave simulation takes about 3 mins. This problem is typically a generative antenna design problem, and prior knowledge is indeed an efficient and effective optimization.

III. PERFORMANCE-LIMIT-GUIDED DECOMPOSITION-BASED MULTIOBJECTIVE OPTIMIZATION FRAMEWORK

This section presents the integration of prior knowledge into the MOEA/D framework [32], enhancing convergence

performance when tackling large-scale mixed-variable multiobjective problems with high computational cost. In particular, the Chu limit is transformed into an explicit Pareto front to guide the optimization process. The performance-limit-guided MOP decomposition and the reference-point solution assignment are employed to direct the algorithm toward the performance limit. Other prior knowledge is also integrated into offspring reproduction and population initialization to further improve algorithm efficiency and effectiveness.

A. Performance-Limit-Guided MOP Decomposition

In decomposition-based multi-objective optimization frameworks, an MOP is decomposed into a set of scalarizing single-objective subproblems, each generated by a scalarizing function with a different weight vector. However, existing studies have shown that the performance of MOEA/D is strongly influenced by the shape and distribution of the underlying Pareto front [38],[39]. This indicates that tailoring the decomposition strategy to the characteristics of the problem's Pareto front can significantly improve algorithmic performance.

In this work, we leverage physical performance limit theory (Chu limit) and relevant engineering constraints to explicitly construct the feasible region and the corresponding true Pareto front in the objective space. These physically grounded Pareto-optimal boundaries are uniformly sampled to generate reference points for subproblem scalarization, enabling the MOEA/D to align more closely with the design problem's intrinsic structure and thereby achieve enhanced convergence and diversity.

1) Performance limit derived from Chu-limit of single mode antenna

Assuming an metallic antenna enclosed by its minimum sphere and dominated by the single mode, the performance limit for given VSWR of s and radiation efficiency η is expressed as follows [20]:

$$BW_{Chu} = \frac{s-1}{\eta\sqrt{s}} \left(\frac{1}{ka} + \frac{1}{(ka)^3} \right)^{-1} \quad (2)$$

where BW_{Chu} is the fractional bandwidth. For metallic antennas, the total efficiency is typically set to 95%, and s is set to 1.93, corresponding to the -10-dB impedance bandwidth. All Chu-limit performance curves in the following sections are derived from (2).

2) Engineering constraints derived from physical size and simulation frequency bounds

In experiments, the antenna structure is enclosed within a sphere of radius R , and its electromagnetic performance is evaluated over a finite frequency range $[f_L, f_U]$. Although the actual antenna topology varies, the boundary of achievable responses can be heuristically estimated by identifying the -10 dB reflection points on both ends, denoted as $P_{-10,L}$ and $P_{-10,R}$, corresponding to the left- and right-hand sides of the frequency response, respectively.

To approximate the engineering constraints, two cases are considered. First, the $P_{-10,L}$ is fixed at f_L , and the $P_{-10,R}$ is swept from f_L to f_U . Second, $P_{-10,R}$ is to fix at f_U , and $P_{-10,L}$ is swept

from f_L to f_U . The relationship between the resulting bandwidth BW and electrical size ka is determined based on these reflection points. Based on these heuristic considerations, the practical engineering constraints $BW_E(ka)$ can be represented by envelope boundaries.

The feasible region $F \subseteq \mathbb{R}^2$ is jointly defined by the derived performance limit $BW_{Chu}(ka)$ and engineering constraints $BW_E(ka)$:

$$\begin{aligned} F = & \{(ka, BW)\} \\ \text{s.t. } & BW \leq BW_{Chu}(ka), BW \leq BW_E(ka), ka_{\min} \leq ka \leq ka_{\max} \end{aligned} \quad (3)$$

To illustrate the feasible region F , the radius R is set to 18.3 mm, and the simulation frequency bound $[f_L, f_U]$ is set from 1.5 to 5 GHz. The boundaries of objective space are shown in Fig. 2. Region 1 represents the feasible region constrained by both performance limit and engineering constraints. Region 2 is the infeasible region beyond the performance limit but within the engineering constraints. Region 3 lies outside both the performance limit and the engineering constraints. Region 4 exceeds engineering constraints but adheres to the Chu limit.

In Fig. 2, the true Pareto front $PF \subseteq F$ is defined by the boundary of the feasible region F (gray region, Region 1), expressed as:

$$\begin{aligned} PF = & \{(ka, BW)\} \\ \text{s.t. } & BW = \min(BW_{Chu}(ka), BW_E(ka)), ka \in [ka_{ZL}, ka_{ZU}] \end{aligned} \quad (4)$$

where ka_{ZL} and ka_{ZU} denote intersection points of $BW_{Chu}(ka)$ and $BW_E(ka)$. The set PF represents the non-dominated frontier, where improvement in one objective necessarily leads to degradation in the other.

The reference points $\mathbf{z} \in PF$ are uniformly distributed points from the derived true Pareto front PF as illustrated in Fig. 4. The k th points $\mathbf{z}^{(k)}$ are utilized to define the k th scalarizing subproblems $g^{(k)}$ in the proposed framework:

$$\min_{\mathbf{x}} g^{(k)}(\mathbf{x}|\mathbf{z}) = \max_{i \in \{1,2\}} (f_i(\mathbf{x}) - z_i^{(k)}), \quad k = 1, \dots, N. \quad (5)$$

where \mathbf{x} is the vector of design parameters, including \mathbf{x}^b and \mathbf{x}^c , and i is the i th objective. The modified Tchebycheff approach ensures that the scalarizing function maintains the diversity of solutions along the irregular Pareto front. By optimizing all N subproblems simultaneously, the method guarantees that if all reference points are reached, the final solutions will exhibit a uniformly distributed and diverse Pareto front.

B. Population-to-Reference-Points Reassignment

The traditional weight vector-based decomposition and cooperation mechanism ensure the MOEA/D can stably converge and maintain the solution diversity along the weight vector direction [40]. In contrast, the reference points-based decomposition proposed in Section II-A provided the explicit convergence targets and allowed global reproduction and solution update.

To further improve convergence, a population reassignment is proposed based on the prior knowledge between reference points and solutions. In practical antenna design, optimal antenna structures at similar center frequencies (electrical size ka in objective space) also tend to be similar. This observation

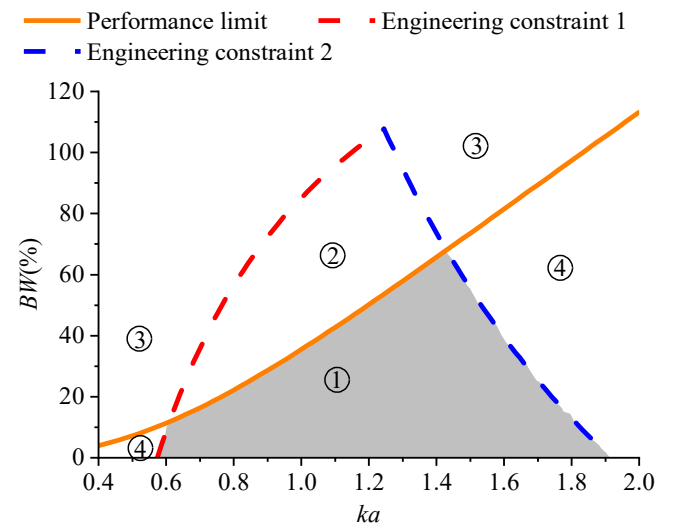


Fig. 3. Feasible region of the proposed optimization problem. The solid line is the true Pareto front derived from the Chu-limit theory. Two dashed lines are engineering constraints derived from physical size and simulation frequency bounds. Four kinds of regions are defined by those boundaries.

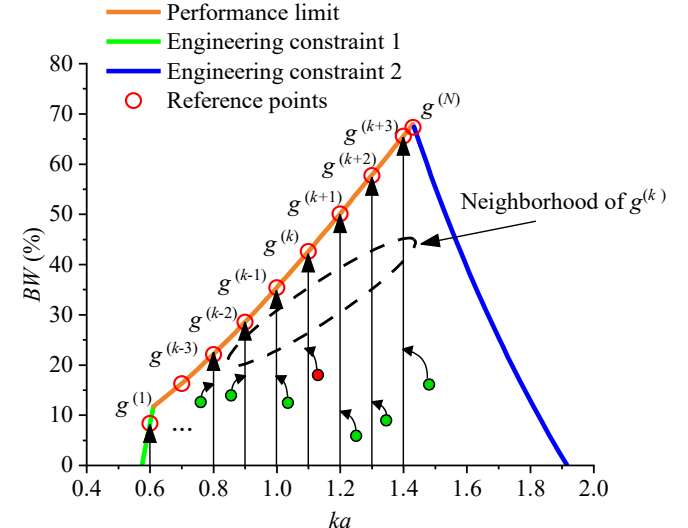


Fig. 4. Illustration of problem decomposition and population reassignment based on derived boundaries. Black solid arrow lines are frequency-based reference lines. Each point is associated with the closest reference line in the objective space. The red point represents the candidate solution, while the green points are identified as neighbors after association.

motivates the proposed population reassignment, which facilitates parent selection and contributes to the generation of high-quality offspring.

The proposed population-to-reference-points reassignment is performed at the beginning of each generation. It mainly follows a two-step procedure: (1) All individuals in the current population are sorted in descending order based on their fractional bandwidth \mathbf{FV}_2 , giving higher priority to those with broadband performance. S is the index set of sorted individuals. (2) Each individual $i \in S$ is then assigned to the subproblem whose reference point is closest in terms of electrical size \mathbf{FV}_1 . The index j of the subproblem corresponds to the i th individual can be obtained as follows:

$$j_i = \arg \min_j |z_i^j - \mathbf{FV}_1^i|, i = s_1, \dots, s_N, s \in S \quad (6)$$

To ensure one-to-one assignment, the selected reference points $\mathbf{z}^{(j)}$ is removed from the candidate set \mathbf{z} once matched. As shown in Fig.4, each dot corresponds to a solution because its location is closest to the corresponding reference line.

The pseudocode of population reassignment is presented in Subalgorithm 1. For each subproblem $g^{(k)}$, neighborhood $\mathbf{B}(k)$ is predefined based on the sequence of reference points. As shown in Fig.4, the red dot represents the solution assigned to the subproblem $g^{(k)}$, while the green dots are assigned to neighboring subproblems. These solutions form the mating pool for offspring reproduction of $g^{(k)}$.

C. Mixed Variable Coding and Offspring Reproduction

In the proposed algorithm framework, each individual \mathbf{x} encodes a candidate ESA structure, and can be represented by an $(M + M \times k)$ -dimensional mixed-variable vector:

$$\mathbf{x} = [x_i^b, \dots, x_M^b, x_{i,1}^c, \dots, x_{i,k}^c, \dots, x_{M,1}^c, \dots, x_{M,k}^c]^T \quad (7)$$

where x_i^b indicates whether the i th metal rod is present ($x_i^b = 1$) or absent ($x_i^b = 0$), and each group $\{x_{i,j}^c\}_{j=1}^k = [x_{i,1}^c, \dots, x_{i,k}^c]$ specifies the geometry and orientation of that rod

Reproduction follows a two-part strategy. The pseudocode is represented in Subalgorithm 2. Binary mutation is applied first, using the DE/rand/1 strategy, to generate a mutated binary vector \mathbf{v}^b . In parallel, the continuous vector \mathbf{x}^c is first mutated using DE/rand/1, followed by polynomial mutation to obtain \mathbf{v}^c . The parent vectors are selected from the neighborhood defined by the population reassignment. A uniform crossover is then performed on the binary variables \mathbf{x}^b and \mathbf{v}^b to generate the offspring \mathbf{u}^b . The associate continuous group $\{x_{i,j}^c\}_{j=1}^k$ for each rod i is inherited from \mathbf{x}^c if $u_i^b = x_i^b$; otherwise, from \mathbf{v}^c . After boundary repair, the offspring is evaluated using a coarse mesh EM model. The process is repeated up to four times or until a valid structure is found.

A key feature of this strategy is the coupling between structural presence and parameter optimization. Each rod's geometry is optimized only when it is active, avoiding unnecessary updates to non-existent structures. The approach reflects a fundamental principle in antenna design: only physical elements that appear in the design affect performance and deserve tuning. At the same time, the parameter dimension remains fixed, with optimization applied only to meaningful structures.

D. Prior-Knowledge Guided Population Initialization

Prior knowledge from the state-of-the-art (SOTA) ESA structures [41]-[44] can effectively guide the generation of high-quality candidates during population initialization. Based on this PK, the probability of generation can be intuitively adjusted to generate structures resembling the SOTA designs, rather than relying on uniform random sampling. A set of prior parameters $\Theta^{prior} = \{p_i\} \cup \{\theta_{i,j}^{prior}\}$ is introduced to construct customized probability distributions. Each x_i^b is sampled from a binary probability distribution $f_b(x_i^b, p_i)$, where p_i represents the activation probability of the i th rod (i.e., $P(x_i^b = 1) = p_i$).

Subalgorithm 1: Population-Reassignment

Input: \mathbf{FV} : function values of current population; \mathbf{z} : initialized reference points

Output: Index: correspondence index between individuals and reference points; \mathbf{S} : sorted index of individuals based on fractional bandwidth.

1. $\mathbf{S} = \text{sort}(\mathbf{FV}_2);$
 2. **for each** i **in** \mathbf{S} **do**
 3. Subproblem index j is obtained by (6)
 4. Delete the reference points $\mathbf{z}^{(j)}$ in \mathbf{z}
 5. $Index(j) = i;$
 6. **end for**
 7. **Return** \mathbf{S} and $Index$
-

Subalgorithm 2: Offspring-Reproduction

Input: \mathbf{P} : the selected parents from the solutions of neighborhood; \mathbf{x} : the current individual

Output: \mathbf{x}' : produced offspring

1. Initialize $i = 1$
 2. **while** $i \leq 4$ or flag = 1 **do**
 3. Perform binary mutation using

$$\mathbf{v}^b = \mathbf{x}^b + \mathbf{F} \cdot (\mathbf{x}_{p1}^b \oplus \mathbf{x}_{p2}^b)$$
 4. Perform continuous mutation using

$$\mathbf{v}^c = \text{PolyMut}(\mathbf{x}^c + F \cdot (\mathbf{x}_{p1}^c - \mathbf{x}_{p2}^c))$$
 5. Apply uniform crossover to \mathbf{x}^b and \mathbf{v}^b to obtain \mathbf{u}^b
 6. Generate \mathbf{u}^c : for each rod i ,

$$\begin{aligned} \text{if } u_i^b = x_i^b &\text{ then } \{u_{i,j}^c\}_{j=1}^k = \{x_{i,j}^c\}_{j=1}^k \\ \{u_{i,j}^c\}_{j=1}^k &= \{v_{i,j}^c\}_{j=1}^k \end{aligned} \text{; else}$$

$$7. \text{Repair } \mathbf{x}' = (\mathbf{u}^b, \mathbf{u}^c) \text{ if out of the boundaries}$$

$$8. \text{Evaluate } \mathbf{x}' \text{ using coarse mesh EM model}$$

$$9. \text{if } \mathbf{x}' \text{ is valid then set flag = 0; else } i=i+1$$

$$10. \text{end while}$$

$$11. \text{Return } \mathbf{x}'$$
-

Subalgorithm 3: Population-Initialization

Input: N : population size; \mathbf{L} : lower bounds of parameters; \mathbf{U} : upper bounds of parameters; Θ^{prior} : prior parameter set

Output: \mathbf{P} : Initialized population

1. **while** $|\mathbf{P}| < N$ **do**
2. **for each** $i = 1$ **to** M **do**
3. Sample $x_i^b \sim f_b(\cdot, p_i)$
4. **for** $j = 1$ **to** k **do**
5. Sample $x_{i,j}^c \sim f_c(\cdot, \theta_{i,j}^{prior})$
6. **end for**
7. $temp = [\mathbf{x}^b, \mathbf{x}^c];$
8. **end for**
9. Evaluate $temp$ using the coarse mesh EM model;
10. if valid then add $temp$ to \mathbf{P} ;
11. **end while**

Each $x_{i,j}^c$ is sampled from a piecewise constant distribution $f_c(x_{i,j}^c, \theta_{i,j}^{prior})$. The prior parameter $\theta_{i,j}^{prior}$ includes the interval bound $[a, b] \subseteq [L_{i,j}^c, U_{i,j}^c]$ and the probability $p(x_{i,j}^c \in [a, b])$ assigned to that interval, to increase probability of sampling the desired geometry and orientation of the i th rod. Therefore, a joint probability distribution $P(\mathbf{x}, \Theta^{prior})$ over the mixed variable vector \mathbf{x} is constructed.

$$P(\mathbf{x}, \boldsymbol{\theta}^{prior}) = \prod_{i=1}^M [f_b(x_i^b, p_i) \cdot \prod_{j=1}^k f_c(x_{i,j}^c, \theta_{i,j}^{prior})] \quad (8)$$

Table I summarizes representative prior settings derived from SOTA ESA designs, illustrating how PK is transformed into the parameters of binary and continuous probability distributions. The pseudocode of population initialization is shown in Subalgorithm 3.

TABLE I
REPRESENTATIVE PRIOR KNOWLEDGE SETTINGS

Prior Knowledge	Affected Variables	High Probability Range
Rods near the driven dipole strongly affect EM response	x_i^b (central region**)	p_i (center region**)
Top-loading rods enhance performance*	x_i^b (top region**), $x_{i,1}^b$ (length), $x_{i,2}^b$ (rotate angle)	p_i (top region**); $p(x_{i,1}^c \in [8,12])$; $p(x_{i,2}^c \in [100,150])$

*The bounds of length and rotate angle are assumed to be [1,12] and [0,180], respectively. **The region is selected by empirical experience.

E. Performance-Limit-Guided MOEA/D Framework

The pseudocode of performance-limit-guided MOEA/D framework is presented in Algorithm 1. Initially, the reference points are uniformly sampled from the derived true Pareto front. Then, the MOP is decomposed into multiple scalarizing subproblems corresponding to reference points (Step 1). Next, a neighborhood set \mathbf{B} is constructed for each reference point by calculating the Euclidean distance among reference points (Step 2-4). The initial population $\mathbf{P}^{(0)}$ is generated using a PK-guided strategy that samples mixed variables from customized probability distributions derived from representative ESA designs (Step 5). The main evolutionary loop iterates until the maximum number of generations (t_{max}) is reached.

Within each generation, three steps are executed:

- Individuals are first sorted by performance and reassigned to the most suitable subproblems using *Population Reassignment*, enabling prioritized mating and better parent selection.
- For the subproblem corresponding to each individual, parents are selected from either the neighborhood or the entire population based on a predefined probability δ , and offspring is generated using *Offspring Reproduction*.
- Each offspring is evaluated against the entire population using scalarizing functions, and up to two solutions are replaced, enabling global update of high-quality solutions.

Eventually, the final population \mathbf{P} is output.

Table II summarizes the PK and their functions in the proposed framework. The positions of PK are also annotated in the framework flowchart shown in Fig. 5. The proposed PK-guided framework introduces two major innovations:

- PK 1 defines the decomposition of the MOP and the construction of the true Pareto front, fundamentally shaping the convergence behavior of the algorithm. With this PK, the algorithm shifts from traditional weight-based guidance to a strategy that focuses on rapidly generating high-quality solutions and globally spreading them across

Algorithm 1: Performance-limit-guided MOEA/D framework

Input: N : population size; T : neighborhood size; t_{max} : maximum number of generations

Output: \mathbf{P} : Final population

- Initialize uniform N reference points ($\mathbf{z}_1, \dots, \mathbf{z}_N$) on True Pareto front derived from Chu-limit theory;
- for each** $i = 1$ to N **do**
- Set $B(i) = \{i_1, \dots, i_T\}$, where $\mathbf{z}_{i_1}, \dots, \mathbf{z}_{i_T}$ are the T closest reference points to \mathbf{z}_i
- end for**
- $\mathbf{P}^{(0)} = \text{Population-Initialization } (N)$;
- for each** generation $t = 1$ to t_{max} **do**
- (\mathbf{S}, Index) = **Population-Reassignment** (\mathbf{P}, FV);
- for each individual** $i \in \mathbf{S}$ **do**
- \mathbf{x}_p selected from the neighborhoods if $rand() < \delta$ else the entire population;
- $\mathbf{x}' = \text{Offspring-Reproduction } (\mathbf{x}_p, \mathbf{x}_i)$
- Update solution of the whole subproblem:
 for each $j \in \mathbf{S}$, set $\mathbf{x}_j = \mathbf{x}'$, if $g(\mathbf{x}' | \mathbf{z}) < g(\mathbf{x}_j | \mathbf{z})$;
- end for**
- end for**
- Return** \mathbf{P} ;

TABLE II
SUMMARY OF PK AND THEIR FUNCTIONS IN THE PROPOSED FRAMEWORK

Prior Knowledge	Function in the Algorithm
PK1 Performance limit and engineering constraints	Guide MOP decomposition using physically bounded true Pareto front
PK2 Structural similarity	Guides solution reassignment based on ka to near center frequency form structure-aware neighborhoods
PK3 Geometry is used only when structure exists	Couple binary and continuous evolution using physical relationship
PK4 Typical structures from SOTA ESA designs	Construct sampling distributions for favor effective designs
PK5 Coarse EM mesh model	Use a fast model to filter out invalid samples

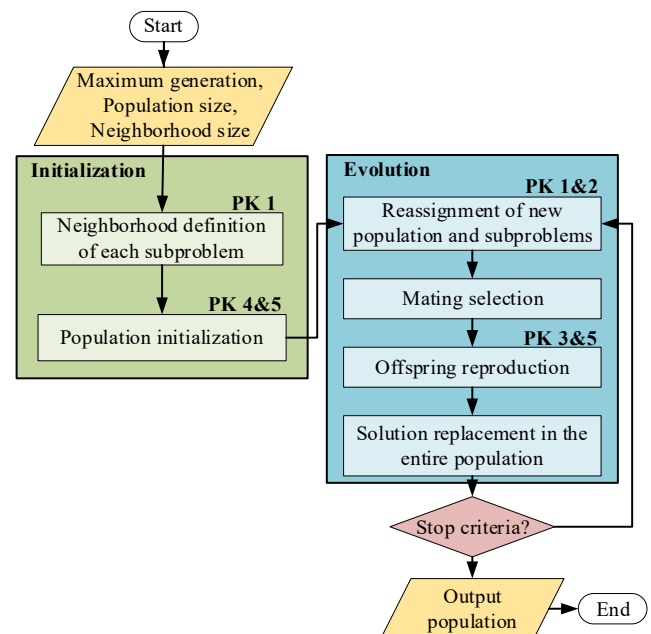


Fig. 5. Flowchart of the proposed optimization framework based on MOEA/D for approaching performance limit of ESA.

the population, thereby accelerating convergence toward subproblem targets.

- PKs 2–5 jointly support the optimization stages across population initialization, parent selection, mixed-variable offspring generation, and fast feasibility screening. This forms a cohesive mechanism that efficiently produces physically meaningful and high-quality solutions.

In essence, the proposed framework modifies MOEA/D using PK to rapid convergence in large scale design spaces.

IV. GENERATIVE ESA DESIGN USING OPTIMIZATION

In this section, we simplified the ESA configuration in Section II-B with prior knowledge constraints for further fabrication and optimized it for approaching performance limit using the proposed algorithm.

A. Prior Knowledge Constraints

The configuration described in Section II-B provides sufficient DoF to generate complex ESA structures. However, to balance design and fabrication feasibility, certain structural parameters that minimally affect EM performance can be further simplified. Two PK constraints are introduced to reduce the dimensionality of the design space, as illustrated in Fig. 6. (1) Constraining metal rods to specific planes. As shown in Fig. 6 (b), the 27 metal rods are divided into three groups, with each group constrained to a specific plane defined by an azimuthal angle ϕ (i.e., $\phi = 0^\circ, 30^\circ, 60^\circ$ in the xoy -plane). Only the elevation angle θ of each rod is adjustable. This plane-constrained arrangement promotes physical connectivity between rods, enabling the effective generation of resonant structures and fabrication feasibility. (2) Adoption of square metal bars with fixed side length. The original metal rods are replaced by square metal bars with a fixed side length, as depicted in Fig. 6(c). This modification minimally affects EM performance but enhances fabrication feasibility.

As demonstrated in Fig. 6, with these PK constraints, the number of parameters is reduced from 135 to 81. The design parameters include 27 binary variables to determine the presence of the metal square bar at the predefined position and 54 continuous variables to control each bar's length and rotation angle. This parameter reduction significantly simplifies the optimization problem while preserving sufficient DoF for performance optimization.

B. Optimization Results

The proposed algorithm is initialized with a population size of 162 individuals and 20 total generations. The 3-D ESA configuration, as shown in Fig. 6, is optimized. Fig. 7 shows the final Pareto front and the population of the 20th generation. Nine solutions in the final Pareto front exceed the fractional bandwidth limit (upper-left boundary) derived from Chu limit [20]. It is evident that these nine individuals distributed along the derived Pareto front demonstrate that the derived PF based on the Chu-limit theory effectively guides the population toward convergence.

Four solutions are selected and illustrated in Fig. 8. The

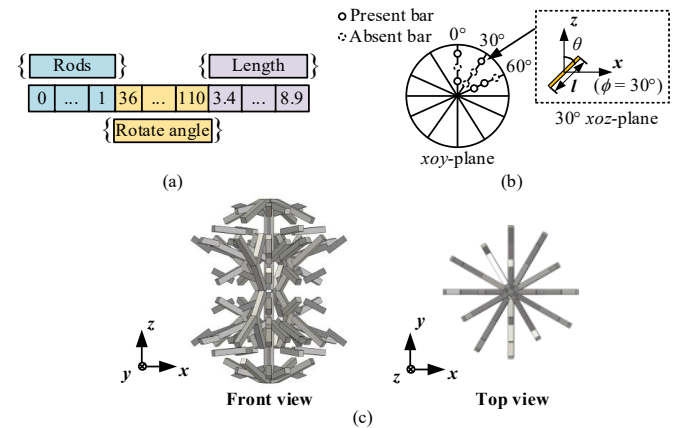


Fig. 6. Simplified 3-D ESA design based on prior knowledge constraints. (a) Representation of design parameter. (b) Fabrication constraints: rods grouped in $\phi = 0^\circ, 30^\circ, 60^\circ$ planes; only θ is adjustable. (c) The front and top views of the generated ESA defined by the above bitstring and constraints.

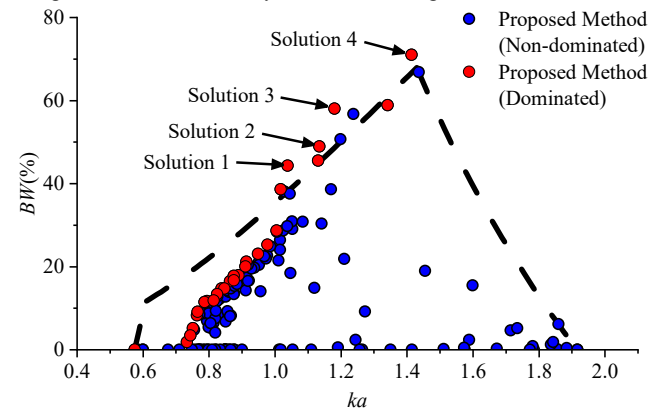


Fig. 7. The optimized results of the proposed method after 20 generations of optimization. Red points indicate the Pareto optimal set (non-dominated solutions), blue points represent the 20th generation result obtained by proposed method.

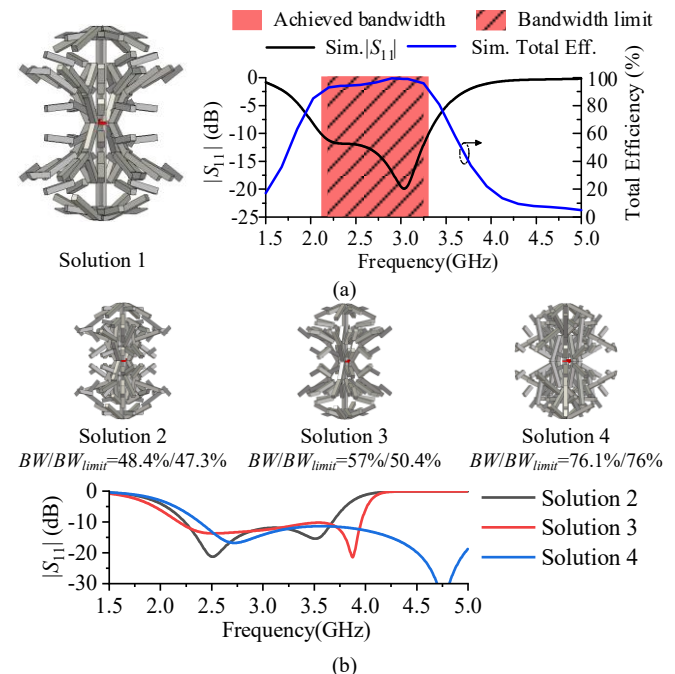


Fig. 8. Antenna structures and the corresponding performance. (a) The antenna structures, $|S_{11}|$ parameter, and total efficiency results of Solution 1. (b) The antenna structures and $|S_{11}|$ parameter results of Solution 2-4.

return loss and total efficiency of Solution 1 are shown in Fig. 8 (a). The simulated impedance bandwidth for $|S_{11}| < -10$ dB is 44.73% (2.1-3.31 GHz), with an electrical size $ka = 1.03$. The average total efficiency within the operating band is 95%. Consequently, the bandwidth-efficiency product ($B\eta$) is 0.425 which exceeds the derived performance limit $B\eta$ of 0.379 at the same ka . The impedance bandwidths of Solution 2-4 are 48.4% (2.24-3.67 GHz), 57% (2.17-3.94 GHz), 76.1% (2.41-5.37 GHz), compared to their respective performance limits of 47.3%, 50.4%, and 76.0%. These solutions demonstrate the effectiveness of the algorithm in generating multiple optimal designs, covering the region of the derived Pareto front for $ka=1-1.4$. The diversity demonstrates the robustness and generalization of the optimization framework, which well balances multiple objectives and constraints to achieve excellent performance in antenna design.

C. Performance Comparison with Baseline Algorithms

The classical NSGA-II and MOEA/D are introduced for performance comparison. To examine the influence of the prior knowledge, all algorithms are applied to the PK-constrained ESA generative design problem defined in Section II and IV-A. To evaluate the performance of the algorithms, the signed inverted generation distance (IGD) metric is utilized. The proposed Chu-limit-guided MOEA/D integrates PK 1-5 in addition to the PK constraint, whereas NSGA-II and MOEA/D are executed only with the PK constraint. For statistical comparison, each algorithm is independently executed five times. The performance limit derived from Section III-A is employed as the Pareto front. The population size of all algorithms is set to $2 \times d$ (i.e. 162), where d is the dimension. The mixed-variable encoding method in NSGA II and MOEA/D is the real-coded strategy. The uniform selection, intermediate crossover, and feasible mutation are utilized in NSGA II by default. The weighted-sum decomposition is utilized in MOEA/D. The population size and neighborhood size are set to be 162 and 20. All algorithms terminate after 20 generations due to the limited simulation budget.

Fig. 9 shows the statistical convergence curves of MOEA/D, NSGA II, and the proposed method over 20 generations. The MOEA/D and NSGA II show a limited reduction in signed IGD within the limited simulation budget, with mean signed IGD values above 0.15. In contrast, the proposed framework exhibits a consistent decrease in signed IGD, reaching values lower than 0.05. This observation is also confirmed in Table III. The proposed method achieves the smallest final signed IGD value of 0.0458 ± 0.0138 among the three algorithms. Meanwhile, the proposed method requires 3718 ± 121 simulations (~37 hours), compared with 3240 simulations (~34 hours) for MOEA/D and NSGA II.

The difference in convergence behavior also appears in the number of beyond-limit solutions obtained. As a result of better convergence, the 9.2 ± 2.7 beyond-limit solutions are obtained from the proposed method, whereas no beyond-limit solution is generated by NSGA II and MOEA/D. The final populations of the best run of the NSGA II and MOEA/D are shown in Fig. 10. There is a notable gap between the performance limit and the

TABLE III
PERFORMANCE COMPARISON BETWEEN MOEA/D, NSGA II, AND THE PROPOSED ALGORITHM

	Proposed algorithm	MOEA/D w/o PK	NSGA II w/o PK
Final IGD value	0.0458 ± 0.0138	0.1841 ± 0.069	0.1595 ± 0.0111
No. of solutions	9.2 ± 2.7	0	0
No. of simulation	3718 ± 121	3240	3240
Simulation time	~37h	~34h	~34h

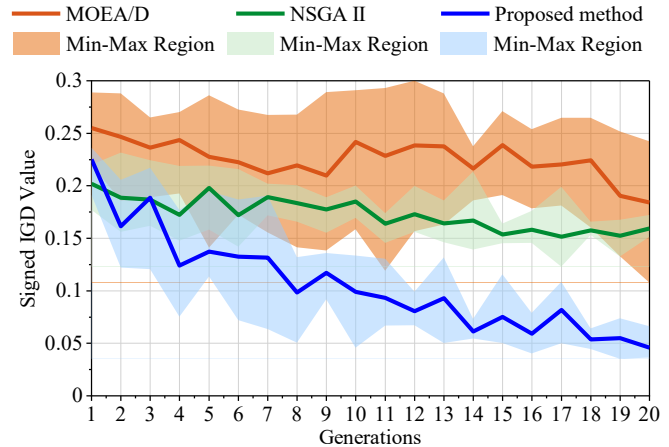


Fig. 9. Statistical convergence curves comparison between MOEA/D, NSGA II, and the proposed algorithm.

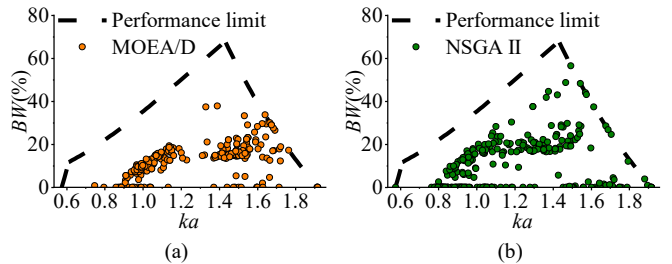


Fig. 10. Final population of (a) MOEA/D and (b) NSGA II.

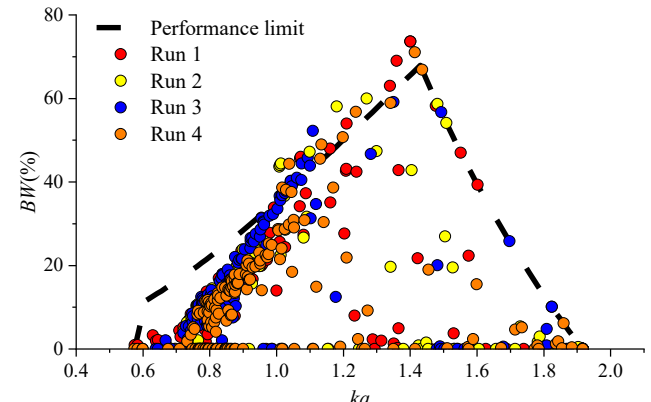


Fig. 11. Final-generation population for four independent runs of the proposed algorithms.

final population of NSGA II and MOEA/D. In contrast, the final populations of the four independent runs of the proposed method are shown in Fig. 11. These four final populations show slightly different distributions for each independent run. Multiple beyond-limit solutions are uniformly covered in the range $ka = 1-1.4$.

V. FABRICATION, EXPERIMENT AND DISCUSSIONS

To validate the effectiveness of the proposed algorithm, Solution 1 is selected for fabrication and measurement.

A. Simplified and equivalent structure for fabrication

The antenna structure of Solution 1, as shown in Fig. 8(a), is hard to fabricate due to the presence of numerous suspend parasitic bars. Based on the mirror theory, the structure of Solution 1, which is a dipole-type structure, can be equivalent to a monopole-like structure, referred to as the “radial-beamlet” antenna. For satisfying the requirement of fabrication, Solution 1 is simplified including removing the suspend bars, smoothing small protrusions, etc. and fabricated by metal 3D printing techniques, as shown in Fig. 12. The printing material based on copper is utilized for ensuring high electrical conductivity, which is Copper-Chromium-Zirconium alloy (CuCrZr, Conductivity $\geq 85\%$ IACS). The $50\ \Omega$ discrete port in the original structure can be equivalent to $25\ \Omega$ coaxial port in the monopole-like structure. The impedance transformer connected to SMA port and $25\ \Omega$ coaxial port is designed with PCB fabrication technique, as shown in Fig. 13.

B. Impedance bandwidth and radiation pattern

The antenna prototype of the fabricated solution is shown in Fig. 14. Fig. 15 shows that the measured and simulated impedance bandwidth for $|S_{11}| < -10\ \text{dB}$ is 54.3% (2.08-3.63 GHz) and 50.3% (2.05-3.43 GHz), respectively. The measured and simulated realized gain over the operating band varies between 1.72-3.86 dBi and 2.14-3.3 dBi, respectively. The simulated directivity over the operating band varies between 3.01-5.1 dBi. The simulated total efficiency is approximately 80%. The good agreement between measured and simulated results shows the effectiveness of the proposed framework. The bandwidth-efficiency product $B\eta$ is 0.402, while the corresponding performance limit $B\eta$ is 0.389.

Table IV summarizes the performance characteristics of the fabricated solution and representative wideband antennas. The calculation of ka does not include the physical size of feeding baluns or large ground planes. For designs [22], [45]-[49] at $ka=0.91-1.07$, the reported designs achieve bandwidths 14%-17.3%. The reported design in [50] and [51] realized 67.7% and 55.6% bandwidth at electrically larger sizes of $ka=1.4$ and 1.73, respectively. The fabricated solution achieves broad bandwidth (50.3%) with high radiation efficiency (80%) at an electrically small size ($ka=1.05$). Meanwhile, the proposed design maintains stable radiation patterns (2.7-3.9 dBi) over its wide operating band. In terms of fabrication complexity, the compared prototypes utilize multilayer substrates [49], NFRP or parasitic loading [45],[46],[48],[51], complex feeding structures [47], or 3D-printed dielectric shells [22],[52]. In contrast, the fabricated solution is realized as metal structure with a simple feeding structure, achieving the highest performance ratio ($R=1.03$) among the designs.

Fig. 16 presents the bandwidth-efficiency product $B\eta$ from Table III against their ka values. The performance limit derived from (2), based on the Chu-sphere, is included for comparison.

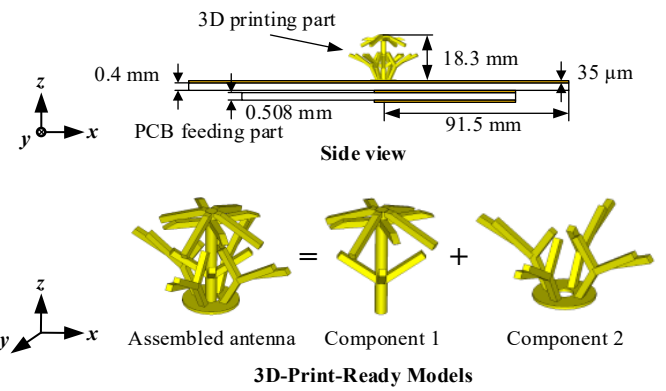


Fig. 12. Configuration of the simplified ESA for fabrication.

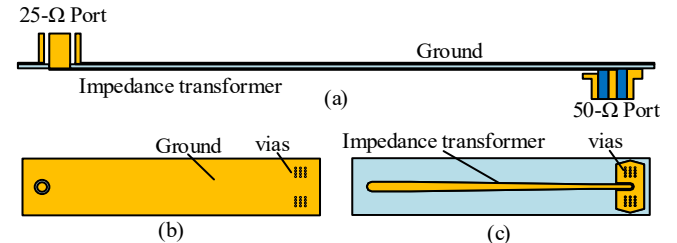


Fig. 13. Configuration of layer 2 in the PCB feeding structure. (a) Side view. (b) Top view. (c) Bottom view.

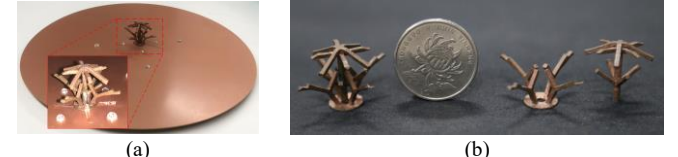


Fig. 14. Photograph of the fabricated ESA. (a) Assembled antenna. (b) Disassembled 3-D printed antenna components.

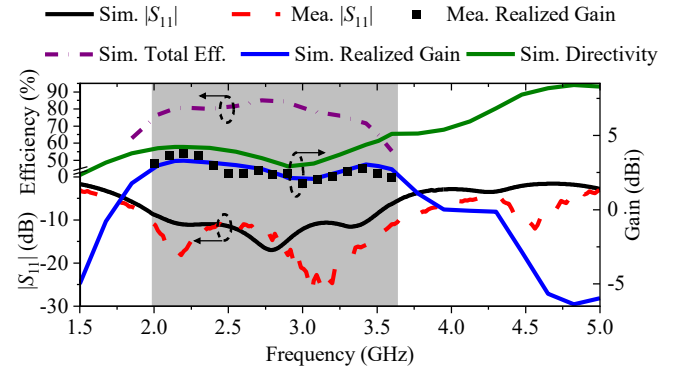


Fig. 15. Simulated and measured reflection coefficient, efficiency, directivity and gain.

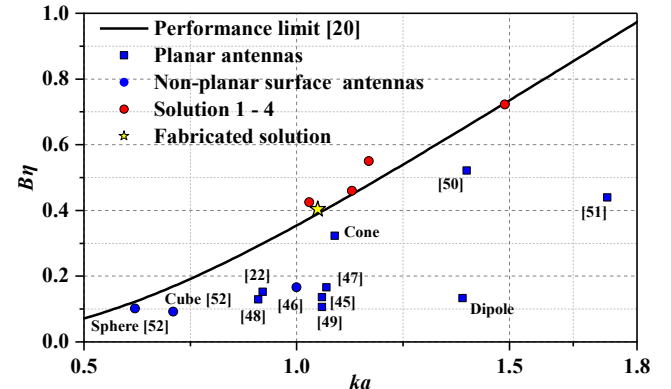


Fig. 16. Comparison of the performance of the recently reported linear polarized wideband antennas to the maximum bandwidth-efficiency product as function of the electrical size ka .

TABLE IV
PERFORMANCE COMPARISON OF THE FABRICATED DESIGN WITH RECENTLY REPORTED LINEAR POLARIZED BROADBAND ANTENNAS

Ref.-Year	ka^*	Size (λ_0^3) [*]	BW (GHz)	Efficiency	Gain (dBi)	Fabrication	R**
[22]-2018	0.92	$4/3 \times \pi \times 0.145^3$	0.666-0.795 (17.9%)	85%	~3.5	3D Printing, ABS resin	0.51
[45]-2020	1.06	$\pi \times 0.168^2 \times 0.002$	2.044-2.36 (14.3%)	95%	0.9-1.5	PCB technique, RO4003C	0.34
[46]-2021	1	$\pi \times 0.168^2 \times 0.001$	1.1-1.31 (17.4%)	95%	~5.5	PCB technique, Rogers 6006	0.47
[50]-2022	1.4	$\pi \times 0.223^2 \times 0.002$	1.31-2.52 (67.7%)	77%	1.68-2.6	PCB technique, RT5880	0.8
[47]-2022	1.07	0.23 \times 0.23 \times 0.001	0.95-1.13 (18%)	92%	1.1-1.6	PCB technique, FR4	0.41
[52]-2023	0.62	$4/3 \times \pi \times 0.098^3$	0.875-0.979 (11.2%)	90%	4.8-6.1	3D printing, ABS300, Sphere	0.83
[52]-2023	0.71	$0.18 \times 0.18 \times 0.13$	0.879-0.976 (10.5%)	87%	4.8-6.5	3D printing, ABS300, Cube	0.54
[48]-2024	0.91	$\pi \times 0.145^2 \times 0.004$	1.5-1.73 (14.2%)	91%	4.4-4.6	PCB technique, Rogers 4350	0.44
[51]-2025	1.73	$0.53 \times 0.12 \times 0.011$	1.62-2.87 (55.6%)	79%	1.6-2.9	PCB technique, RO4003	0.48
[49]-2025	1.06	$\pi \times 0.166^2 \times 0.068$	1.85-2.13 (14%)	76%	2.9-4.2	Multilayer PCB, Rogers 6006	0.27
Fabricated Solution***	1.05	$4/3 \times \pi \times 0.167^3$	2.08-3.63 (54.3%)	80%	2.7-3.9	3D Printing, All copper	1.03

* λ_0 and k are calculated at the center frequency of the operating bandwidth in free space. ** $R = BW \cdot \eta / (BW \cdot \eta)_{Chu}$, calculated from the performance limit given in (2). *** Fabricated solution is simplified and fabricated based on Solution 1.

The dipole and cone references are simulated with the same physical size as the proposed design. A notable performance gap is observed between the reported designs and the performance limit. Most reported designs [45]-[49] are low-profile planar structures, whose limited volume utilization leads to reduced performance compared with the performance limit. The reported design [52] is closer to the performance limit, owing to its more efficient utilization of the 3D region. It is immediately apparent that the $B\eta$ of the fabricated solution and optimized solutions 1-4 above and closely follow the performance limit. It validates the effectiveness and scalability of the proposed algorithm framework.

To explicitly highlight the trade-offs of the fabricated design, the specific merits and limitations of the reported designs are summarized as follows:

Advantages: (1) Beyond-limit performance. The fabricated solution approaches the performance limit by a balance between small electrical size and wide impedance bandwidth. (2) Algorithm-driven generality. Using a generic all-metal 3D-printed radiator with a simple feeding, the proposed framework relies on the optimization algorithm to systematically discover multiple unintuitive antenna structures. It demonstrates strong scalability beyond conventional design.

Limitations: (1) Spherical design region. To approach the performance limit, the proposed antenna is designed in the spherical region with high profile. It increases fabrication difficulty and restricts applicability in low-profile industrial scenarios. (2) Practical implementation. The optimized dipole-like solution is validated by converting it into an equivalent monopole-like structure. The introduction of a ground plane and feeding network leads to performance loss, such as realized gain and radiation efficiency.

Overall, despite the implementation trade-offs, the fabricated solution verifies the beyond-limit performance and its improvement over the reported works. It demonstrates that the solutions generated by the proposed framework are physically valid and can be experimentally realized. These observations provide a solid foundation for further mechanism exploration and for advancing practical applications. Furthermore, this enables a new design paradigm of data-driven knowledge discovery, in which high-performance designs are generated to initiate the investigation of novel radiation mechanisms.

VI. CONCLUSIONS

A Chu limit-guided decomposition-based multiobjective optimization technique has been developed. The Pareto front derived from the performance limit and engineering constraints was utilized to decompose the multiobjective problem into multiple single objective subproblems. Other prior knowledge was incorporated at different stages of the proposed framework to efficiently generate effective solutions. Using the proposed algorithm, the ESA with high DoF has been optimized, and the multiple solutions exceeding the performance limit have been obtained. One solution has been simplified and fabricated. The fabricated solution achieves measured and simulated impedance bandwidth ($|S_{11}| < -10$ dB) of 54.3% (2.08-3.63 GHz) and 50.3% (2.05-3.43 GHz), respectively. The measured and simulated realized gain over the operating band vary between 1.72-3.86 dBi and 2.14-3.3 dBi, respectively. The multiple solutions obtained from the proposed framework demonstrate the effectiveness of the generative antenna design concept for pursuing the performance limit.

REFERENCES

- [1] L. J. Chu, "Physical limitations of omni-directional antennas," *J. Appl. Phys.*, vol. 19, no. 12, pp. 1163-1175, 1948.
- [2] H. A. Wheeler, "Fundamental limitations of small antennas," *Proc. IRE*, vol. 35, no. 12, pp. 1479-1484, 1947.
- [3] A. D. Yaghjian and S. R. Best, "Impedance, bandwidth, and Q of antennas," *IEEE Trans. Antennas Propag.*, vol. 53, no. 4, pp. 1298-1324, 2005.
- [4] C. Pfeiffer, "Fundamental efficiency limits for small metallic antennas," *IEEE Trans. Antennas Propag.*, vol. 65, no. 4, pp. 1642-1650, 2017.
- [5] A. D. Yaghjian and H. R. Stuart, "Lower bounds on the Q of electrically small dipole antennas," *IEEE Trans. Antennas Propag.*, Article vol. 58, no. 10, pp. 3114-3121, 2010.
- [6] R. Collin and S. Rothschild, "Evaluation of antenna Q ," *IEEE Trans. Antennas Propag.*, vol. 12, no. 1, pp. 23-27, 1964.
- [7] W. Geyi, "Physical limitations of antenna," *IEEE Trans. Antennas Propag.*, vol. 51, no. 8, pp. 2116-2123, 2003.
- [8] M. Gustafsson, C. Sohl, and G. Kristensson, "Illustrations of new physical bounds on linearly polarized antennas," *IEEE Trans. Antennas Propag.*, vol. 57, no. 5, pp. 1319-1327, 2009.
- [9] M. Gustafsson, C. Sohl, and G. Kristensson, "Physical limitations on antennas of arbitrary shape," *Proceedings of the Royal Society A: Mathematical, Physical and Engineering Sciences*, vol. 463, no. 2086, pp. 2589-2607, 2007.
- [10] B. P. Nel, A. K. Skrivervik, and M. Gustafsson, " Q -factor bounds for microstrip patch antennas," *IEEE Trans. Antennas Propag.*, vol. 71, no. 4, pp. 3430-3440, 2023.

- [11] S. R. Best, "Low Q electrically small linear and elliptical polarized spherical dipole antennas," *IEEE Trans. Antennas Propag.*, vol. 53, no. 3, pp. 1047-1053, 2005.
- [12] H. L. Thal, "New radiation Q limits for spherical wire antennas," *IEEE Trans. Antennas Propag.*, vol. 54, no. 10, pp. 2757-2763, 2006.
- [13] A. B. Murray and A. K. Iyer, "An exact synthesis procedure for minimum quality factor spherical wire antennas," *IEEE Trans. Antennas Propag.*, vol. 73, no. 4, pp. 2308-2318, 2025.
- [14] M. Capek *et al.*, "Optimal planar electric dipole antennas: Searching for antennas reaching the fundamental bounds on selected metrics," *IEEE Antennas Propag. Mag.*, vol. 61, no. 4, pp. 19-29, 2019.
- [15] S. R. Best, "Electrically small resonant planar antennas: Optimizing the quality factor and bandwidth," *IEEE Antennas Propag. Mag.*, vol. 57, no. 3, pp. 38-47, 2015.
- [16] O. S. Kim, O. Breinbjerg, and A. D. Yaghjian, "Electrically small magnetic dipole antennas with quality factors approaching the Chu lower bound," *IEEE Trans. Antennas Propag.*, vol. 58, no. 6, pp. 1898-1906, 2010.
- [17] H. R. Stuart and A. D. Yaghjian, "Approaching the lower bounds on Q for electrically small electric-dipole antennas using high permeability shells," *IEEE Trans. Antennas Propag.*, vol. 58, no. 12, pp. 3865-3872, 2010.
- [18] R. W. Ziolkowski and A. Erentok, "Metamaterial-based efficient electrically small antennas," *IEEE Trans. Antennas Propag.*, vol. 54, no. 7, pp. 2113-2130, 2006.
- [19] A. D. Yaghjian, "Reducing the Q lower bound for electrically small antennas using dispersive tuning," *IEEE Trans. Antennas Propag.*, vol. 72, no. 5, pp. 4642-4646, 2024.
- [20] D. F. Sievenpiper *et al.*, "Experimental validation of performance limits and design guidelines for small antennas," *IEEE Trans. Antennas Propag.*, vol. 60, no. 1, pp. 8-19, 2012.
- [21] E. E. Altshuler, "Electrically small self-resonant wire antennas optimized using a genetic algorithm," *IEEE Trans. Antennas Propag.*, vol. 50, no. 3, pp. 297-300, 2002.
- [22] M.-C. Tang, X. Chen, M. Li, and R. W. Ziolkowski, "Particle swarm optimized, 3-D-printed, wideband, compact hemispherical antenna," *IEEE Antennas Wirel. Propag. Lett.*, vol. 17, no. 11, pp. 2031-2035, 2018.
- [23] J. Tucek, M. Capek, L. Jelinek, and O. Sigmund, "Density-based topology optimization in method of moments: Q -factor minimization," *IEEE Trans. Antennas Propag.*, vol. 71, no. 12, pp. 9738-9751, 2023.
- [24] M. Capek, L. Jelinek, and M. Gustafsson, "Shape synthesis based on topology sensitivity," *IEEE Trans. Antennas Propag.*, vol. 67, no. 6, pp. 3889-3901, 2019.
- [25] L. Jelinek and M. Capek, "Optimal currents on arbitrarily shaped surfaces," *IEEE Trans. Antennas Propag.*, vol. 65, no. 1, pp. 329-341, 2017.
- [26] M. Capek, M. Gustafsson, and K. Schab, "Minimization of antenna quality factor," *IEEE Trans. Antennas Propag.*, vol. 65, no. 8, pp. 4115-4123, 2017.
- [27] M. Gustafsson and S. Nordebo, "Optimal antenna currents for Q , superdirectivity, and radiation patterns using convex optimization," *IEEE Trans. Antennas Propag.*, vol. 61, no. 3, pp. 1109-1118, 2013.
- [28] P. Liu, L. Chen, and Z. N. Chen, "Prior-knowledge-guided deep-learning-enabled synthesis for broadband and large phase shift range metacells in metalens antenna," *IEEE Trans. Antennas Propag.*, vol. 70, no. 7, pp. 5024-5034, 2022.
- [29] Y. Lyu, T. H. Gan, and Z. N. Chen, "TE-TM balanced wide-angle metacells for low scan-loss metalens antenna using prior knowledge-guided generative deep learning-enabled method," *IEEE Trans. Antennas Propag.*, pp. 1-1, 2025.
- [30] P. Liu and Z. N. Chen, "Full-range amplitude-phase metacells for sidelobe suppression of metalens antenna using prior-knowledge-guided deep-learning-enabled synthesis," *IEEE Trans. Antennas Propag.*, vol. 71, no. 6, pp. 5036-5045, 2023.
- [31] Y. Tian *et al.*, "Evolutionary large-scale multi-objective optimization: A survey," *ACM Comput. Surv.*, vol. 54, no. 8, pp. 1-34, 2021.
- [32] Q. Zhang and H. Li, "MOEA/D: A multiobjective evolutionary algorithm based on decomposition," *IEEE Trans. Evol. Comput.*, vol. 11, no. 6, pp. 712-731, 2007.
- [33] Q.-Q. Li, Q.-X. Chu, Y.-L. Chang, and J. Dong, "Tri-objective compact log-periodic dipole array antenna design using MOEA/D-GPSO," *IEEE Trans. Antennas Propag.*, vol. 68, no. 4, pp. 2714-2723, 2020.
- [34] D. Lu, L. Wang, E. Yang, and G. Wang, "Design of high-isolation wideband dual-polarized compact MIMO antennas with multiobjective optimization," *IEEE Trans. Antennas Propag.*, vol. 66, no. 3, pp. 1522-1527, 2018.
- [35] X. Wang, G. Wang, D. Wang, and Q. Zhang, "Ensemble-learning-based multiobjective optimization for antenna design," *IEEE Trans. Antennas Propag.*, vol. 71, no. 2, pp. 1295-1303, 2023.
- [36] J. Nagar and D. H. Werner, "A comparison of three uniquely different state of the art and two classical multiobjective optimization algorithms as applied to electromagnetics," *IEEE Trans. Antennas Propag.*, vol. 65, no. 3, pp. 1267-1280, 2017.
- [37] D. Ding and G. Wang, "Modified multiobjective evolutionary algorithm based on decomposition for antenna design," *IEEE Trans. Antennas Propag.*, vol. 61, no. 10, pp. 5301-5307, 2013.
- [38] Y. Qi, X. Ma, F. Liu, L. Jiao, J. Sun, and J. Wu, "MOEA/D with adaptive weight adjustment," *Evol. Comput.*, vol. 22, no. 2, pp. 231-64, 2014.
- [39] H. Ishibuchi, Y. Setoguchi, H. Masuda, and Y. Nojima, "Performance of decomposition-based many-objective algorithms strongly depends on pareto front shapes," *IEEE Trans. Evol. Comput.*, vol. 21, no. 2, pp. 169-190, 2017.
- [40] Y. Yuan, H. Xu, B. Wang, and X. Yao, "A new dominance relation-based evolutionary algorithm for many-objective optimization," *IEEE Trans. Evol. Comput.*, vol. 20, no. 1, pp. 16-37, 2016.
- [41] C. Friedman, "Wide-band matching of a small disk-loaded monopole," *IEEE Trans. Antennas Propag.*, vol. 33, no. 10, pp. 1142-1148, 1985.
- [42] H. R. Stuart, S. R. Best, and A. D. Yaghjian, "Limitations in relating quality factor to bandwidth in a double resonance small antenna," *IEEE Antennas Wirel. Propag. Lett.*, vol. 6, pp. 460-463, 2007.
- [43] K. Fang-Yao, C. Hsi-Tseng, H. Heng-Tung, C. Hsi-Hsir, and P. Nepa, "A novel dipole antenna design with an over 100% operational bandwidth," *IEEE Trans. Antennas Propag.*, vol. 58, no. 8, pp. 2737-2741, 2010.
- [44] T.-H. Yang and D. F. Sievenpiper, "Intuitive broadband matching technique for top-loaded monopole antennas," *IEEE Trans. Antennas Propag.*, vol. 67, no. 12, pp. 7611-7616, 2019.
- [45] X. Chen, M. C. Tang, D. Yi, and R. W. Ziolkowski, "Wideband, electrically small, near-field resonant parasitic dipole antenna with stable radiation performance," *IEEE Antennas Wirel. Propag. Lett.*, Article vol. 19, no. 5, pp. 826-830, 2020.
- [46] X. Chen, M.-C. Tang, D. Yi, and R. W. Ziolkowski, "Wideband, compact antennas with interdigitated magnetic-based near-field resonant parasitic elements," *IEEE Trans. Antennas Propag.*, vol. 69, no. 8, pp. 5036-5041, 2021.
- [47] Y. Zhang and Y. Li, "Wideband isotropic antenna with miniaturized ground for enhanced 3 db coverage ratio," *IEEE Antennas Wirel. Propag. Lett.*, vol. 21, no. 6, pp. 1253-1257, 2022.
- [48] Y. Wang, M.-C. Tang, M. Li, D. Li, and X. Zeng, "Planar single-layer wideband electrically small quasi-isotropic antenna characterized by filtering response," *IEEE Trans. Antennas Propag.*, vol. 72, no. 2, pp. 1363-1372, 2024.
- [49] Q. Lin, M.-C. Tang, M. Li, and R. W. Ziolkowski, "Electrically small, enhanced bandwidth, low-profile, broadside-radiating huygens dipole antenna," *IEEE Antennas Wirel. Propag. Lett.*, pp. 1-5, 2025.
- [50] Q. Lin, M.-C. Tang, X. Chen, D. Yi, M. Li, and R. W. Ziolkowski, "Low-profile, electrically small, ultrawideband antenna enabled with an inductive grid array metasurface," *IEEE Trans. Antennas Propag.*, vol. 70, no. 8, pp. 7152-7157, 2022.
- [51] Y. Wang *et al.*, "Design of a mode-compressed wideband asymmetrical dipole antenna with stable omnidirectional radiation pattern," *IEEE Trans. Antennas Propag.*, vol. 73, no. 3, pp. 1882-1887, 2025.
- [52] R. Wang, K. Klionovski, and A. Shamim, "Fully printed 3-D antennas with wideband radiation isotropy based on annular currents models," *IEEE Open J. Antennas Propag.*, vol. 4, pp. 484-491, 2023.



Yu Kuang (S'20-M'25) received the B.Eng. degree in communication engineering from Southern University of Science and Technology (SUSTech), Shenzhen, China, in 2019, and the Ph.D. degree from the National University of Singapore (NUS), Singapore, in 2025.

He was a Postdoctoral Fellow with Southern University of Science and Technology, Shenzhen, China, in 2025. He is currently an ARTIC Fellow with the National University of Singapore.

He was a recipient of the Best Student Paper Award at the 2023 Asia-Pacific Conference on Antennas and Propagation (APCAP). His current research interests include metantennas, characteristic mode analysis, electrically small antennas, optimization, and deep learning.



Qingsha S. Cheng (S'00-M'05-SM'09) received the B.Eng. and M.Eng. degrees from Chongqing University, Chongqing, China, in 1995 and 1998, respectively, and the Ph.D. degree from McMaster University, Hamilton, ON, Canada, in 2004.

In 1998, he joined the Department of Computer Science and Technology, Peking University, Beijing, China. In 2004, he became a Postdoctoral Fellow and, in 2007, a Research Engineer with the Department of Electrical and Computer Engineering, McMaster University. In 2014, he joined the Department of Electrical and Electronic Engineering, Southern University of Science and Technology (SUSTech), Shenzhen, China, where he is currently an Associate Professor.

He has authored or coauthored more than 200 publications including technical book chapters, refereed international technical journals, refereed international conference proceedings, and international workshops. His current research interests include AI-assisted and physics-driven smart modeling and optimization of microwave components and antennas, surrogate modeling and optimization, space mapping, multiobjective optimization, and neural networks.



Zhi Ning Chen (M'99-SM'05-F'07) received his B.Eng, M.Eng, and Ph.D degrees all in Electrical Engineering from the Institute of Communications Engineering (ICE), China in 1985, 1988, and 1993, and his second PhD degree in 2003 from the University of Tsukuba, Japan, respectively.

In 2012, he joined the Department of Electrical and Computer Engineering, National University of Singapore (NUS), as a tenured Full Professor. Currently, he is a Provost Chair Professor and the founder and Director of the Advanced Research and Technology Innovation Center. Prior to NUS, he worked at ICE as a Lecturer and later as a Professor, and at Southeast University, China, as a Postdoctoral Fellow and later an

Associate Professor from 1988 to 1995. From 1995 to 1997, he joined the City University of Hong Kong (HK) as a Research Assistant and later a Research Fellow. Between 1997 and 1999, he conducted his research at the University of Tsukuba, Japan, with the Japan Society for the Promotion of Science (JSPS) Fellowship Award. In 2001 and 2004, he visited the University of Tsukuba twice under the JSPS Fellowship Program (senior level). In 2004, he worked at IBM T. J. Watson Research Center, Yorktown, USA, as an Academic Visitor. In 2013, he visited the "Laboratoire des Signaux et Systèmes," UMR8506 CNRS-Supelec-University Paris Sud in Gif-sur-Yvette, France, as a Senior DIGITEO Guest Scientist. In 2015, he visited the Center for Northeast Asian Studies of Tohoku University, Japan, as a Senior Visiting Professor. From 1999 to 2016, he worked with the Institute for Infocomm Research (I²R) (formerly Centre for Wireless Communications, National University of Singapore), Singapore, as a Principal Scientist, Department Head, Manager, and Technical Advisor. In 2023, he visited Chalmers University of Technology, Sweden under E2 Guest Researcher Program.

Dr. Chen held concurrent guest professorships at Southeast University (Changjiang Chair Professor), Nanjing University, Tsinghua University, Shanghai Jiaotong University, Tongji University, University of Science and Technology of China, Fudan University, Dalian Maritime University, Chiba University, National Taiwan University of Science and Technology, National Taiwan University, South China University of Technology, Shanghai University, Beijing University of Posts and Telecommunications, Yunnan University, Beijing Institute of Technology, Nanyang Technologies University, University of Surrey, City University of Hong Kong, and Chalmers University of Technology.

Dr. Chen is currently serving as a member of the State Key Laboratory of Millimeter-waves at Southeast University and the State Key Laboratory of Tera-Hertz & Millimeter-waves at City University of Hong Kong. Additionally, he has served as a reviewer for local and overseas research organizations in Canada, Chile, mainland China, Hong Kong SAR, Finland, Ireland, Sweden, and the UK.

Dr. Chen has provided technical consultancy services to twelve local and overseas companies as a Technical Advisor, Guest Professor, and Chief Scientist.

Dr. Chen is the founding General Chair of the Marina Forum (Mar-For in 2021), International Workshop on Antenna Technology (iWAT in 2005), International Symposium on InfoComm & Mechatronics Technology in Bio-Medical & Healthcare Application (IS 3T-in-3A in 2010), International Microwave Forum (IMWF in 2010), and Asia-Pacific Conference on Antennas and Propagation (APCAP in 2012). He has also been involved in multiple international events as General Chair, as well as Chair and member of Program Committees and Advisory committees. He is the General Chair of the 2021 IEEE International Symposium on Antennas and Propagation and USNC-URSI Radio Science Meeting (the first version outside North America).

Dr. Chen has been invited to deliver 190+ keynote, plenary, and invited speeches at international academic and industrial events.

Dr. Chen has published 729(J351+C378) academic papers and seven books entitled Broadband Planar Antennas (Wiley 2005),

UWB Wireless Communication (Wiley 2006), Antennas for Portable Devices (Wiley 2007), Antennas for Base Stations in Wireless Communications (McGraw-Hill 2009), Handbook of Antenna Technologies (with 76 chapters) (Springer References 2016 as Editor-in-Chief), and Substrate-Integrated Millimeter-Wave Antennas for Next-generation Communications and Radars (Wiley and IEEE Press Series on Electromagnetic Wave Theory in 2021). He has also contributed chapters to the books entitled Developments in Antenna Analysis and Design (IET 2018), UWB Antennas and Propagation for Communications, Radar, and Imaging (Wiley 2006), Antenna Engineering Handbook (McGraw-Hill 2007), Microstrip and Printed Antennas (Wiley 2010), and Electromagnetics of Body Area Networks (Wiley 2016).

Dr. Chen holds 35 granted and filed patents and has completed 43+ technology licensing deals with industry.

Dr Chen is a pioneer in developing small and wideband and ultra-wideband antennas, wearable and implanted medical antennas, package antennas, near-field antennas and coils, three-dimensional integrated LTCC arrays, microwave lens antennas, and microwave metamaterial-metasurface antennas for communications, sensing, and imaging systems. Currently, Dr. Chen is more interested in the translational research of electromagnetic metamaterials and the applications of characteristic mode analysis, transformation optics, and prior-knowledge-guided deep learning-enabled optimization and generative design methods in antenna engineering.

Dr. Chen is the recipient of the prestigious IEEE Antennas and Propagation Society (APS) John Kraus Antenna Award in 2021, EurAAP Antenna Award 2025, and the International Symposium on Antennas and Propagation Best Paper Award in 2010, the CST University Publication Awards in 2008 and 2015, the ASEAN Outstanding Engineering Achievement Award in 2013, the Institution of Engineers Singapore Prestigious Engineering Achievement Awards in 2006, 2013 (two awards), and 2014, the I²R Quarterly Best Paper Award in 2004, the IEEE iWAT Best Poster Award in 2005, several technology achievement awards from China during 1990-1997, as well as more than 28 academic awards received by the students under his supervision.

Dr. Chen was elevated to the Fellow of the Academy of Engineering, Singapore in 2019, the Fellow of the IEEE for his contributions to small and broadband antennas for wireless applications in 2007, and Fellow and Vice President of the Asia-Pacific Artificial Intelligence Association. Currently, he is serving as a member of the IEEE APS AdCom and the IEEE Future Networks Initiative Technology Focus Editorial Board. He has served the IEEE Council on RFID as a member of Fellow Committee, aDistinguished Lecturer since 2016 and as a founding Vice President during 2015-2020. He served the IEEE Transactions on Antennas and Propagation as an Associate Editor and the IEEE APS as a Distinguished Lecturer, as well as a member of the Fellow Committee and the New Direction Committee, now a member of Administration Committee and Meetings Committe. He served as the Chair of the IEEE Singapore MTT/AP Chapter in 2008 and the Chair of the IEEE Singapore RFID Chapter in 2017.

(www.ece.nus.edu.sg/staff/bio/czn.html)